

Continuum Robot Deflection under External Loads and Prescribed Tendon Displacements

Kaitlin Oliver-Butler *Student Member, IEEE*, John Till *Student Member, IEEE*, and Caleb Rucker *Member, IEEE*

Abstract—Soft and continuum robots driven by tendons or cables have wide-ranging applications, and many mechanics-based models for their behavior have been proposed. Here we address the unsolved problem of predicting robot deflection due to environmental loads while the axial displacements of the tendon ends are held constant. We first solve this problem analytically for a tendon-embedded Euler-Bernoulli beam. Dimensionless plots describe how tendon stiffness and routing path affect the robot’s output compliance at any point along its length. Designs with converging tendons have increased stiffness. Generalizing to curved shapes and large deflections in 3D, we extend a Cosserat-rod-based model for tendon-driven robots to handle prescribed tendon displacements, tendon stretch, pretension, and slack. We then provide dimensionless plots in the actuated case for loads in 3D. The analytical formulas and numerically-computed model are experimentally validated on a prototype robot with good agreement. Error from static friction is relatively low but increases for shapes with higher curvatures. The results enable stiffness analysis of candidate robot designs without significant modeling effort.

I. INTRODUCTION

From applications in surgery to safe human-robot interaction, soft and continuum robots have been increasingly proposed and researched over the last decade [1]–[4]. For these flexible manipulators, tendons or cables have been one of the primary actuation paradigms, and tendon-driven continuum systems have been used for surgery [5]–[7], space applications [8], [9], and humanoid robots [10]. A key advantage of a cable/tendon transmission is that the driving actuators can be grounded off of the robot structure, thus facilitating smaller and more agile manipulator designs.

It is well known that in the absence of external loads from the environment, a continuum robot segment with a uniform cross section and straight, parallel tendon routing paths conforms to a constant-curvature shape when actuated [2], [4], [11], but when under external loads, the shape deforms and no longer exhibits constant curvature. Mechanics-based static and dynamic models of the externally loaded behavior have been derived and validated by several groups [12]–[18]. However, the shape a robot takes when under environmental loads strongly depends on how the proximal tendon ends are controlled during loading. For example, the tendon tensions could be held constant throughout the external load application

This material is based upon work supported by the National Science Foundation under CMMI-1427122 as part of the NSF/NASA/NIH/USDA/DOD National Robotics Initiative and was funded in part by the National Science Foundation under CAREER Award #1652588. Any opinion, findings, and conclusions or recommendations expressed in this material are those of the authors and do not necessarily reflect the views of the National Science Foundation.

K. Oliver-Butler, J. Till, and D. C. Rucker are with the University of Tennessee, Knoxville, TN 37996, USA (e-mail: caleb.rucker@utk.edu).

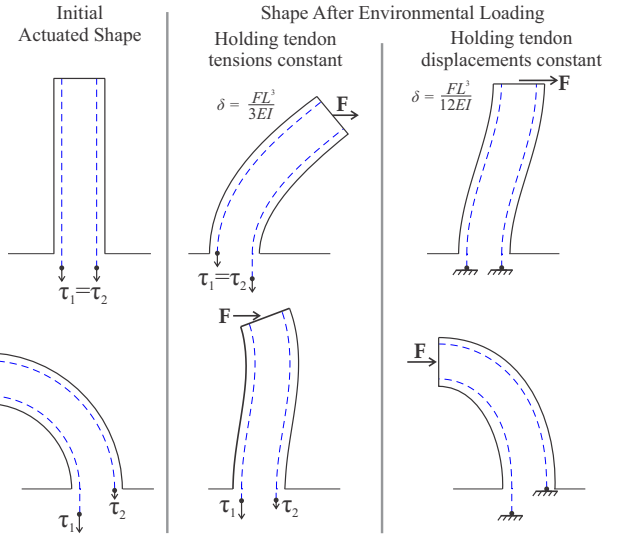


Fig. 1. Above is an example result from our analysis. The deflection of a tendon-actuated robot under environmental loading varies significantly depending on whether tendon tensions or the tendon attachment points are considered constant during load application. In this paper, we analyze robot deflection under environmental loads and prescribed tendon displacements, studying the effects of design parameters such as tendon axial stiffness and routing path.

or otherwise dictated by a monitored tension control system (e.g. [19], [20]), or the axial displacements of the proximal tendon end could be dictated and held constant by a servo actuation system. These two cases generate very different deflection behavior, as illustrated in Figure 1. When the tensions are held constant, external loading will cause a change in the proximal tendon displacements. When the proximal displacements are held constant, the external loading will change the tendon tension, and this generally makes the robot have a lower output compliance. While constant-curvature kinematics models without external loads are generally based on prescribed tendon lengths (e.g. [2], [11], [21], [22]), all existing models for externally-loaded robots have assumed tendon *tensions* are the prescribed inputs to the system; none seek to answer the question of what happens when the axial tendon displacements are prescribed and held fixed during environmental loading, aside from a brief exploration in [23]. This historic modeling emphasis on prescribed tension inputs is somewhat incongruous with the majority of robotic systems themselves (e.g [5], [9], [11], [16], [24]–[26]) which have commonly used non-backdrivable, servo-actuation systems that receive high-level position commands and prescribe the associated tendon displacements, even if the actuation tension is ultimately measured.

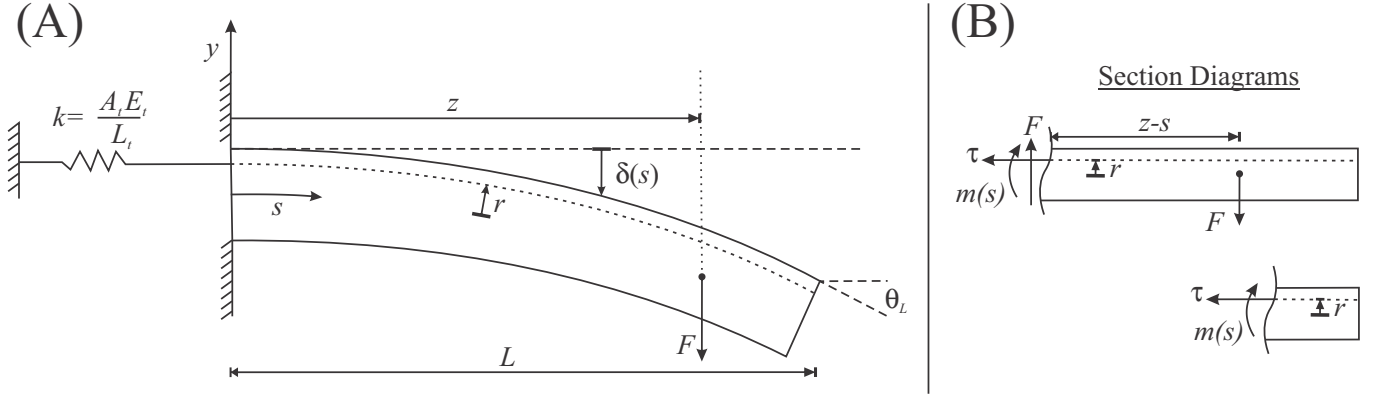


Fig. 2. Problem schematic (A) and free-body diagrams (B) used to derive the analytical results, shown here with exaggerated deflections for clarity.

A. Outline and Contributions

In this paper, we seek to remedy this imbalance by providing models that can predict the deflection of tendon-displacement-controlled continuum robots under environmental loads. In Section II, we begin by deriving simple models for the loaded deflection of initially straight, Bernoulli-Euler beams that are constrained by displacement-controlled tendons. This analysis provides analytical formulas and dimensionless plots that enable an intuitive understanding of the role of tendon stiffness, routing path radius, backbone compressibility, and load location on the beam's deflection curve. These results should be generally useful for predicting and adjusting the properties of a continuum manipulator during the design process. We further analytically describe the potential stiffness benefits of non-parallel tendon routing. We provide additional deflection formulas for this more general case in Section III, and we show that routing paths that converge to the neutral axis at the tip of a robot segment can markedly improve stiffness. Section IV extends the coupled Cosserat rod/tendon model of [14] to include prescribed displacement inputs, tendon stretch, and nonlinear slack, which we accomplish by modifying the algorithmic structure and boundary conditions of the original model. This extended model is then implemented to produce simulation results for external loading of an actuated robot segment in 3D to extend and further illuminate the principles of Sections II and III. In Section V, we experimentally validate the derived deflection formulas and the extended Cosserat model by measuring the response of prototype structures to a set of known loading conditions. Section VI discusses our results and considers possible future work.

II. ANALYTICAL RESULTS FOR SMALL DEFLECTIONS WITH PARALLEL TENDON ROUTING

In this section, we use classical beam theory to derive expressions for the deflection of an elastic member under a transverse external load. The member contains ideal flexible tendons passed through frictionless guide channels along its length and affixed at the tip and the base of the member (i.e. a prescribed displacement of zero), as depicted in Figure 2 for a single tendon. Note that this derivation differs from the conventional analysis of a beam with non-homogeneous cross section. Here, the tendon material is allowed to slide axially

within its channel, whereas different material layers are not permitted to slide with respect to one another in a simple non-homogeneous beam. We analyze only the straight “unactuated” state and assume small deflections from it. These assumptions allow us to obtain simple analytical deflection formulas that can inform intuition about more complex, actuated scenarios and guide general design choices. We consider (1) a single extensible tendon running parallel to the member’s central line, (2) the limiting case of an inextensible tendon, (3) backbone compression, and (4) multiple pretensioned tendons. In Section V, we provide experimental validation of our derived deflection formulas.

A. Analysis with a Single Stretchable Tendon

The schematic in Figure 2 depicts the variables in our problem statement. An initially straight, cantilevered elastic member of length \$L\$, Young’s modulus \$E\$, and second area moment \$I\$ is subjected to a force at a distance \$z\$ from the base. Arc length along the member is denoted by \$s\$. A flexible tendon runs through a straight channel at a radial distance \$r\$ from the center. The proximal tendon end is fixed in space, and the tendon has a total spring constant \$k\$, which is given in the figure by the classical formula for axial stiffness in terms of tendon cross sectional area \$A_t\$, Young’s modulus \$E_t\$, and length \$L_t\$. The tendon channel is assumed to be frictionless, which implies that the tendon tension is constant along the length. For now, we assume the tendon is relaxed when the member is straight, and in tension when the external load is applied, but we will consider pretension later when we examine the case of multiple tendons. If the tendon is pulled, the member will bend, but our present aim is only to examine the effect that tendon elasticity and radial location has on the deflection from this nominal straight state under external loads.

Examining the free-body section diagrams in Figure 2, we can write a static moment balance and solve for the internal moment (about the \$x\$ axis) as a function of arc length. Assuming small deflection, we obtain

$$m(s) = \begin{cases} F(s - z) + r\tau & \text{if } s < z \\ r\tau & \text{if } s \geq z \end{cases} \quad (1)$$

We assume the classical linear constitutive law that the internal moment is proportional (via the flexural rigidity \$EI\$) to the rate

of change of the tangent angle with respect to arc length,

$$m(s) = -EI \frac{d\theta}{ds}, \quad (2)$$

where the negative comes from the sign conventions established in Figure 2. Then integrating the moment equation, enforcing the boundary condition $\theta(0) = 0$, and enforcing continuity in $\theta(s)$ at $s = z$, we get

$$-EI\theta(s) = \begin{cases} \frac{1}{2}Fs^2 + (r\tau - Fz)s & \text{if } s < z \\ r\tau s - \frac{1}{2}Fz^2 & \text{if } s \geq z. \end{cases} \quad (3)$$

At this point, the tendon reaction tension is unknown, but we can obtain it from the tendon stretch caused by the deflection of the beam $\Delta = r\theta_L$ and the tendon spring constant k as

$$\tau = kr\theta_L. \quad (4)$$

Substituting the above into (3) and evaluating at $s = L$, we can solve for θ_L and obtain

$$\theta_L = \frac{Fz^2}{2(EI + r^2kL)}, \quad (5)$$

and consequently,

$$\tau = \frac{Fkrz^2}{2(EI + r^2kL)}. \quad (6)$$

Note that the F and r vectors are designated positive in opposite directions in Figure 2, and the tension will be positive if this is the case. If not, then the tension computed by the above expression will be negative, indicating compression, which is impossible for an ideal flexible tendon. Thus, application of this analysis must be restricted to cases with either positive tension or tendons that can support some compressive force without buckling (e.g. metal rods). With multiple tendons, pretension can be applied to ensure all the tensions remain positive during subsequent external loading, and we analyze this case in the latter part of this section.

Finally, making the small angle approximation $\theta \approx \frac{d\delta}{ds}$, we can integrate once more, enforce the boundary condition $\delta(0) = 0$, and enforce continuity of $\delta(s)$ at $s = z$ to obtain

$$-EI\delta(s) = \begin{cases} \frac{1}{6}Fs^3 + \frac{1}{2}(r\tau - Fz)s^2 & \text{if } s < z \\ \frac{1}{2}r\tau s^2 - \frac{1}{2}Fz^2s + \frac{1}{6}Fz^3 & \text{if } s \geq z. \end{cases} \quad (7)$$

Equation (7), when combined with (6), is the most general form of our result in this section, providing deflection as a function of arc length, load magnitude, load location, total member length, flexural rigidity, tendon location, and tendon stiffness. However, examining some special cases of this result can also provide some useful insight that can be encapsulated in simpler formulas. For instance, we can consider the deflection at the same location where the lateral loading is applied ($s = z$). In this case, we get

$$\delta(z) = \frac{Fz^3}{3EI} - \left(\frac{r^2kz}{EI + r^2kL} \right) \frac{Fz^3}{4EI}. \quad (8)$$

For the special case of tip loading ($z = L$), the tip deflection is

$$\delta_{tip} = \frac{FL^3}{3EI} - \left(\frac{r^2kL}{EI + r^2kL} \right) \frac{FL^3}{4EI}. \quad (9)$$

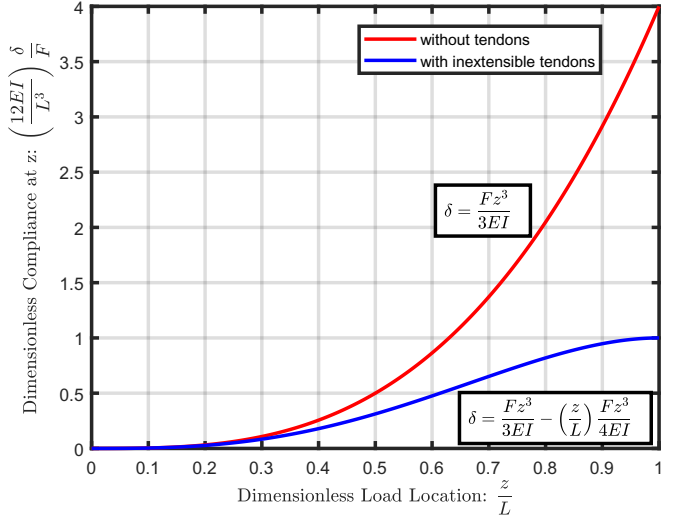


Fig. 3. With reference to Figure 2, this plot shows our derived nondimensional relationship between the load's distance z from the base and the deflection δ at the point of loading. The red line depicts the classical formula for the deflection of a solid elastic member while the blue line shows our new result for the deflection of a member with inextensible actuation tendons.

We see that the classical cantilevered deflection formula $\frac{FL^3}{3EI}$ appears as the first term, and that δ_{tip} is equal to this in the case of $k = 0$ (no tendon) or $r = 0$ (tendon located at the centerline). Increasing either k or r will tend to reduce the deflection (increase the effective stiffness at the tip), and the dependence on r^2 is illuminating for the purposes of design; increasing r by a factor of 2 has the same effect as increasing k by factor of 4.

To illustrate our results in a generally useful way throughout the paper without specifying manipulator or material properties, we define the following dimensionless quantities, representing tendon stiffness, compliance at the loaded point, and load location, respectively:

$$\alpha := \frac{r^2kL}{EI} \quad \sigma := \left(\frac{12EI}{L^3} \right) \frac{\delta}{F} \quad \zeta := \frac{z}{L}.$$

The nondimensional form of Equation (8) is then

$$\sigma = 4\zeta^3 - 3 \left(\frac{\alpha}{1 + \alpha} \right) \zeta^4. \quad (10)$$

When $\zeta = 1$, this equation becomes the dimensionless form of Equation 9. These dimensionless quantities will be used as the axes of our plots in this paper, but we will label them using the full dimensionless expressions for clarity. We plot the above relationship of dimensionless tip compliance versus dimensionless tendon stiffness for a parallel tendon in Figure 7 compared to a converging tendon design developed Section III. The plot shows that the robot's dimensionless tip compliance approaches an asymptote of 1 as the tendon stiffness increases to infinity.

B. Inextensibility

Many models assume the tendons are inextensible (such as the model in [27]), as there are various cable materials with a sufficiently high stiffness, and we can consider the effect of

having an inextensible tendon by letting $k \rightarrow \infty$. In this case, we see that

$$\lim_{k \rightarrow \infty} \theta_L = 0,$$

and the deflection at the loaded point is

$$\delta(z) = \frac{Fz^3}{3EI} - \left(\frac{z}{L}\right) \frac{Fz^3}{4EI}. \quad (11)$$

We plot this relationship nondimensionally in Figure 3. From this, we see that the tip deflection in response to loads at the tip is

$$\delta_{tip} = \frac{FL^3}{12EI}, \quad (12)$$

which is depicted in Figure 1. This is exactly one fourth of the deflection experienced by the same member with no tendons. Interestingly, and somewhat counter-intuitively, the reaction tension of an *inextensible* tendon in response to transverse external loading is only a function of the path radius, total length, and the loading; it is not influenced by the member's flexural rigidity:

$$\lim_{k \rightarrow \infty} \tau = \frac{Fz^2}{2rL}. \quad (13)$$

In contrast, the tension required to actively bend the member to a certain angle in free space is proportional to the flexural rigidity.

C. Backbone Compression

The prior formulas consider only members with an incompressible backbone, but for "soft" manipulators and some catheter robots, the effects of backbone compression are non-negligible [9], [25]. To model these cases, we define the total compression force on the backbone c_B as

$$c_B = -k_B \Delta_B = \tau, \quad (14)$$

where k_B is the axial backbone stiffness and Δ_B is the axial stretch of the backbone. This affects the stretch of the tendon Δ . Without backbone compression, $\Delta = r\theta_L$, but including it makes

$$\Delta = \Delta_B + r\theta_L. \quad (15)$$

The reaction tension can be found by substituting (14) and (15) into $\tau = k\Delta$ and isolating τ . This leads to the tip angle as a function of backbone and tendon stiffness:

$$\theta_L = \frac{Fz^2}{2(EI + r^2 L k_{eq})}, \quad (16)$$

where

$$k_{eq} = \frac{k_B k}{k_B + k}. \quad (17)$$

Equation (16) is the same form as Equation (5) with a different tendon stiffness value. Similarly, expressions for tendon tension τ and the deflection of the loaded point $\delta(z)$ are the same form as in the incompressible case except with $k = k_{eq}$, implying that a compressible backbone acts like a spring in series with an extensible tendon in this single-tendon case. Thus, an equivalent stiffness can be used in the equations presented for the inextensible case in order to handle an axially compliant backbone.

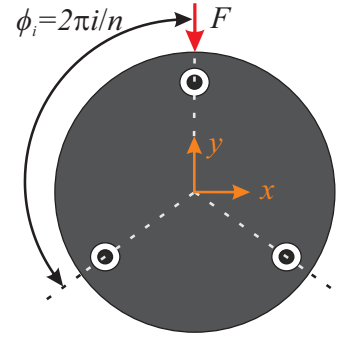


Fig. 4. Cross section of a continuum robot with equally spaced tendons.

D. Multiple Pretensioned Tendons

The above analysis assumed only a single, initially relaxed tendon. However, continuum robots and tendon-actuated catheters usually employ at least two tendons for bending in a plane and often three or four symmetrically spaced tendon channels for bending in two planes, as shown in Figure 4. For three or more equally spaced tendons, the deflection of an initially straight, symmetric member will be in the direction of the lateral load vector, and the deflection will be equal for unit loads in all lateral directions. If there are $n > 2$ equally spaced, equally pretensioned tendons at equal radii r from the centroidal axis with equal k and equal pretension τ_p , then the internal moment in the direction perpendicular to the lateral load in the cross sectional plane is

$$m(s) = \begin{cases} F(s - z) + rT & \text{if } s < z \\ rT & \text{if } s \geq z, \end{cases} \quad (18)$$

where

$$T = \sum_{i=1}^n \cos\left(\frac{2\pi i}{n}\right) \tau_i,$$

and τ_i is the tension of the i^{th} tendon in response to the load, including any pretension. The trigonometric term accounts for the perpendicular distance from the bending plane to the tendon location in the cross section. In terms of the deflected tip angle θ_L and the pretension τ_p (equal for all tendons so that the initial shape is straight), the individual reaction tension τ_i is given by

$$\tau_i = kr \cos\left(\frac{2\pi i}{n}\right) \theta_L + \tau_p. \quad (19)$$

This is also the correct expression in the case of multiple tendons with a compressible backbone as long the pretension is high enough for all tendons to remain in positive tension during loading. In the interest of space, we do not prove this here, but it follows from a similar analysis as the previous section.

By inspection, we see that all terms involving τ_p cancel out in T due to the trigonometric coefficients and the equal spacing of the tendons. Thus, pretension has no effect on the internal moment and no effect on the displacement under load. Pretension could increase static frictional forces and thus indirectly affect stiffness, and it can also eliminate slack tendons, as we show in Section IV. However, under the ideal

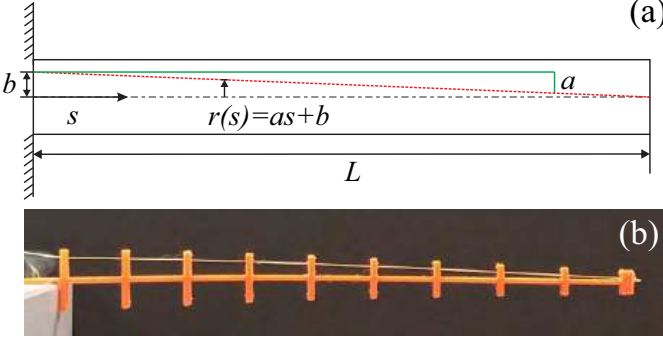


Fig. 5. A nonparallel tendon routing path is defined by a linear function of s . The diagram (a) and a prototype (b) depict the particular choice of $a=-b/L$, which results in the tendon path converging to the backbone center at the tip of the segment.

assumptions of no friction and no slack, one cannot make a tendon-driven manipulator with an elastic, passive backbone stiffer by increasing tendon pretension, which has also been observed by Kim et al [28]. Exceptions to this include some multi-link structures in [28] and pneumatic backbone structures that stiffen with a combination of increased pressure and tension [29].

The rest of the derivation follows the single tendon case, and our result for the displacement at the loaded point is

$$\delta(z) = \frac{Fz^3}{3EI} - \left(\frac{r^2 kz \sum_{i=1}^n \cos^2 \phi_i}{EI + r^2 kL \sum_{i=1}^n \cos^2 \phi_i} \right) \frac{Fz^3}{4EI}, \quad (20)$$

where

$$\phi_i = \frac{2\pi i}{n}$$

as defined in Figure 4. This confirms the intuitive result that adding more tendons can increase stiffness, but the upper limit of tip stiffness given by Equation (12) still holds, even if infinitely many tendons are used.

Again, this result assumes all tendons remain in tension during deformation, which is achievable through an appropriate constant pretension. In the worst-case scenario for potential slack, where the member deflects purely in the direction of a single tendon, the required pretension to prevent slack in that tendon is the same as in Equation (6). All other tendons will undergo smaller deflections and will thus not experience slack given equal pretension.

III. NONPARALLEL LINEAR TENDON PATHS

Motivated by the intriguing but limited result that parallel inextensible tendons increase the stiffness of an elastic member by a factor of four, we now seek to explore whether further stiffness gains may be obtained by considering tendon paths that do not run parallel to the member's central axis or to each other. We derive similar formulas to those obtained in the previous section for parallel tendons, considering inextensibility, multiple pretensioned tendons, and the effect that nonparallel tendon routing has on the manipulator shape and required actuation force.

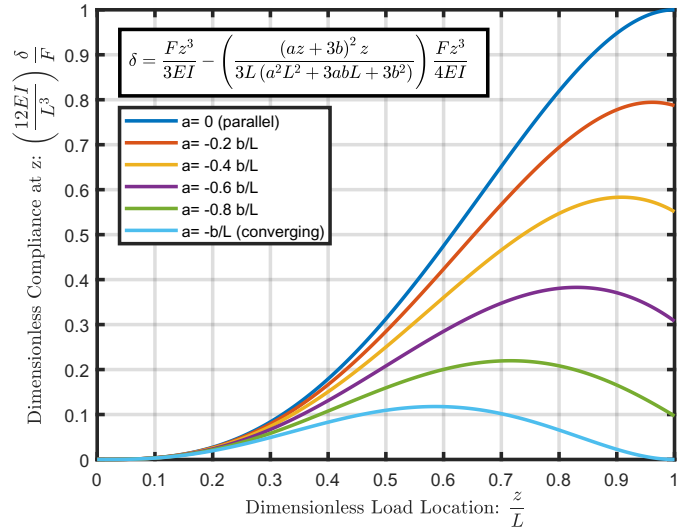


Fig. 6. This plot shows the nondimensional relationship between a load's distance z from the base and the deflection δ at the point of loading for multiple slopes of nonparallel tendon routing cases, where the tendons are assumed to be inextensible. The line with a value of $a = 0$ depicts our result for the deflection of a member with inextensible parallel tendons, as in Figure 3 (but note the y-axis scaling difference). Increasing the slope means terminating the tendon closer to the member's centerline, which this plot shows will increase overall stiffness. The bottommost line, where $a = -b/L$, represents a tendon that is terminated at the centerline, and the compliance is exactly zero for loads at the tip under the assumption of inextensible tendons.

We let the tendon channel radius be a linear function of s (as shown in Figure 5) and restate Equation (1):

$$m(s) = \begin{cases} F(s-z) + r(s)\tau & \text{if } s < z \\ r(s)\tau & \text{if } s \geq z, \end{cases} \quad (21)$$

where $r(s) = as + b$, a is the slope of the tendon path, and b is the initial radius at the base. After applying the constitutive law in Equation (2), integration of (21) and enforcement of the boundary condition $\theta(0) = 0$ and continuity in $\theta(s)$ at $s = z$ yields

$$-EI\theta(s) = \begin{cases} \frac{1}{2}(F + a\tau)s^2 + (b\tau - Fz)s & \text{if } s < z \\ \frac{1}{2}a\tau s^2 + b\tau s - \frac{1}{2}Fz^2 & \text{if } s \geq z. \end{cases} \quad (22)$$

Given the initial assumption of small deflections, we additionally assume that $a \equiv \frac{dr}{ds} \ll 1$, and thus the total tendon stretch Δ (assuming backbone incompressibility) is

$$\Delta = \int_0^L r(s) \left(\frac{d\theta}{ds} \right) ds, \quad (23)$$

where $\frac{d\theta}{ds} = -\frac{m(s)}{EI}$. Integrating this and once more enforcing the boundary conditions and continuity gives

$$\Delta = \frac{1}{EI} \left[\frac{Fa}{6} z^3 + \frac{Fb}{2} z^2 - \left(\frac{a^2 L^2}{3} + abL + b^2 \right) \tau L \right]. \quad (24)$$

The tendon reaction tension can then be calculated as $\tau = k\Delta$, resulting in

$$\tau = \frac{kF(az^3 + 3bz^2)}{6EI + kL(2a^2L^2 + 6abL + 6b^2)}. \quad (25)$$

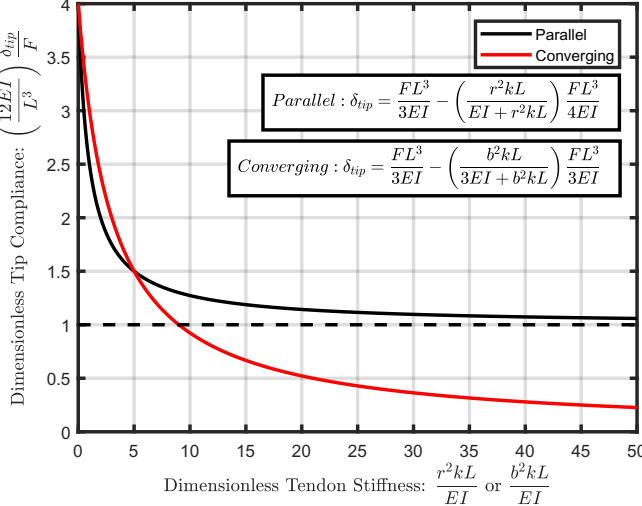


Fig. 7. This plot shows the relationship between a tendon's stiffness and the deflection response to a tip load for both parallel routing and converging routing. Tendon stretch plays a larger role when a tendon is routed in a converging manner, but as the tendon stiffness increases, the robot tip compliance goes to zero (infinite stiffness).

Substituting the tension into (22) and once more integrating, we obtain the final deflection formula:

$$-EI\delta(s) = \begin{cases} \frac{1}{6}(F + a\tau)s^3 + \frac{1}{2}(b\tau - Fz)s^2 & \text{if } s < z \\ \frac{1}{6}a\tau s^3 + \frac{1}{2}b\tau s^2 - \frac{1}{2}Fz^2s + \frac{1}{6}Fz^3 & \text{if } s \geq z. \end{cases} \quad (26)$$

Thus, the deflection of the loaded point is

$$\delta(z) = \frac{Fz^3}{3EI} - \frac{\tau}{6EI} (az^3 + 3bz^2), \quad (27)$$

and for tip loading,

$$\delta_{tip} = \frac{FL^3}{3EI} - \frac{\tau}{6EI} (aL^3 + 3bL^2), \quad (28)$$

where τ is given by (25). When the tendons are assumed to be inextensible, these equations become:

$$\delta(z) = \frac{Fz^3}{3EI} - \left(\frac{(az + 3b)^2 z}{3L(a^2 L^2 + 3abL + 3b^2)} \right) \frac{Fz^3}{4EI} \quad (29)$$

and

$$\delta_{tip} = \frac{FL^3}{3EI} - \left(\frac{(aL + 3b)^2}{3(a^2 L^2 + 3abL + 3b^2)} \right) \frac{FL^3}{4EI}. \quad (30)$$

The plot in Figure 6 shows how increasing the magnitude of the slope a can increase the overall stiffness of the manipulator, where all other variables remain unchanged.

A. Converging Tendon Path

Figure 6 reveals a special case of nonparallel tendon routing that has zero tip compliance, which we have named converging routing; in this case, the tendon path begins at a radial offset of b at the base and ends at the neutral axis centerline at the tip, meaning that $a = -b/L$. As shown by Figure 5, the backbone and the tendon form a truss-like structure, illustrating why this design has significantly greater resistance to tip loads

compared to parallel tendon designs. For a single converging tendon, the deflection at the loaded point simplifies to

$$\delta(z) = \frac{Fz^3}{3EI} - \left(\frac{(3bLz^2 - bz^3)^2}{3EI + b^2 kL} \right) \frac{kF}{12L^2 EI}, \quad (31)$$

and the deflection of the end for a tip load is

$$\delta_{tip} = \frac{FL^3}{3EI} - \left(\frac{b^2 kL}{3EI + b^2 kL} \right) \frac{FL^3}{3EI}. \quad (32)$$

Fig. 7 depicts the relationship between tip compliance and tendon stiffness in dimensionless form for this style of routing, compared to the same formula for parallel tendons from Section II. Whereas the parallel tendon case has an asymptotic tip compliance of 1, with converging tendons the tip compliance actually approaches zero as tendon stiffness is increased. This confirms that a converging tendon design could be significantly stiffer than a parallel tendon design with all other factors equal, as long as the effective tendon stiffness is high enough. For dimensionless tendon stiffness greater than 5, a converging-tendon robot will be stiffer than a parallel tendon robot.

B. Converging Tendon Inextensibility

Assuming the tendons can be considered inextensible, the deflection equation reduces further:

$$\delta(z) = \frac{Fz^3}{3EI} - \left(\frac{z}{L} \right) \left(\frac{3L - z}{\sqrt{3L}} \right)^2 \frac{Fz^3}{4EI}. \quad (33)$$

Figure 6 depicts Equation (33) (converging) and Equation (11) (parallel, previously graphed as the blue line in Figure 3) alongside other tendon slope values using this deflection formula. The deflection with converging routing is smaller than the parallel case regardless of the load location, and of particular interest is its ability to handle tip loads, as it produces a tip deflection of zero regardless of the load magnitude:

$$\delta_{tip} = \frac{FL^3}{3EI} - \left(\frac{2L}{\sqrt{3L}} \right)^2 \frac{FL^3}{4EI} = 0. \quad (34)$$

This is obviously an impractical result, as some tendon stretch is inevitable, and the effective tendon stiffness must be very high in order to approach this behavior according to Figure 7. Regardless, the stiffness can be markedly improved; this is shown experimentally in Section V, where converging tendons increased stiffness by almost a factor of 2 versus parallel tendons (i.e. a factor of 8 improvement over the member's stiffness with no tendons).

C. Multiple Pretensioned Converging Tendons

For multiple pretensioned tendons that take a converging path, the derivation for the deflection begins similarly to the parallel case with Equation (18), where the radius r is defined as $r(s) = as + b$ and $a = -b/L$. The definition of T is then

$$T = \sum_{i=1}^n (k\Delta_i + \tau_p) \cos \phi_i, \quad (35)$$

where ϕ_i is defined in Figure 4,

$$\Delta_i = \Delta \cos \phi_i,$$

and Δ is as defined in Equation (23). Again, the pretension terms cancel out in T due to the trigonometric factor and the equal spacing, and the derivation follows what has been previously done. The resulting formula for the deflection of the loaded point is

$$\delta(z) = \frac{Fz^3}{3EI} - \left(\frac{(3bLz^2 - bz^3)^2 \sum_{i=1}^n \cos^2 \phi_i}{3EI + b^2 k L \sum_{i=1}^n \cos^2 \phi_i} \right) \frac{kF}{12L^2 EI}. \quad (36)$$

D. Routing Effects on Actuation, Shape, and Design

The significant stiffness advantage of converging routing, especially the theoretically infinite tip stiffness for inextensible tendons, raises the question of whether there is any significant tradeoff associated with a converging tendon design. In particular, one might suspect that the required actuation force for articulation of the tip in free space might be increased by a converging tendon path. In order to characterize this, we examine the deflection equations without an external load for both tendon path cases. Taking Equations (3) and (22), we set the load force to zero, set $s = L$, and reverse the sign convention on θ for convenience of expression to find actuation forces. The parallel tendon actuation force required to achieve a particular tip angle θ_L in free space is

$$\tau_{parallel} = \frac{EI}{rL} \theta_L. \quad (37)$$

In contrast, the required actuation force for the converging path is

$$\tau_{converging} = 2 \frac{EI}{bL} \theta_L. \quad (38)$$

For two members that have the same initial base offset, (i.e., $b = r$), the converging tendon member requires twice the actuation force of the member with parallel routing to achieve the same tip angle.

If we compare the tension required to achieve the same tip displacement δ_L in free space, the tradeoff is less significant. Based on Equations (7) and (26), the required tensions are

$$\tau_{parallel} = \frac{2EI}{rL^2} \delta_L \quad (39)$$

and

$$\tau_{converging} = \frac{3EI}{bL^2} \delta_L. \quad (40)$$

Thus, the converging tendon case only requires 50% greater actuation force beyond the parallel case. The relative stiffness gain, however, could potentially be much greater according to Figure 7, and actuation systems with higher force capacity and positional precision can easily be designed to handle the increased requirements.

The routing also affects the actuated and deflected shapes of the manipulator. The actuated shape of a parallel-routed manipulator is constant curvature, which has been explored extensively and summarized in [2]. With a converging tendon path, actuation creates a shape with linearly varying curvature

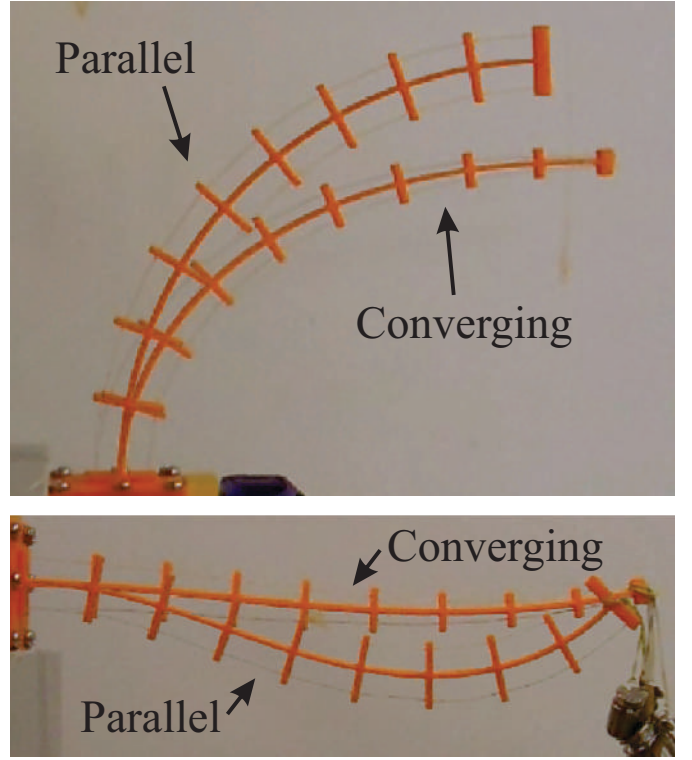


Fig. 8. (Top) Both manipulators are actuated to a tip angle of 90° with the constant-curvature shape of the parallel-routed manipulator shown against the linearly-varying curvature shape of the converging-tendon manipulator. The parallel manipulator required a tendon displacement 7.1% of its total length to reach this position while the converging manipulator required 5.3%. (Bottom) This overlay shows the results when the manipulators were placed under a 0.9 N tip load and actuated back to the zero position as closely as possible. Clearly, the manipulator with converging tendons recovered its shape much better than the one that has parallel tendons.

(higher curvature at the base) due to the linearly varying moment arm of the tendon. This shape is identical to the shape of a simple cantilevered beam under tip load (for small deflections) because a tip load also creates a linearly varying internal moment. Figures 19 and 23 in Section V show the shape of an externally-loaded manipulator for both path routing cases. The deflected shape in the parallel case is s-shaped (maintaining approximately constant tip angle) while the s-shape is less pronounced in the converging design.

The images in Figure 8 were taken from the attached video, which also demonstrates shape variations caused by routing choices. In the first set of clips, both a parallel- and converging-tendon manipulator are actuated to $\pm 90^\circ$ tip angles. The parallel-path manipulator produces the expected constant-curvature shape, but it requires more tendon displacement and less tension to reach the tip angle than does the converging-routed one. The second set of clips show both initially straight manipulators placed under a 0.9 N tip load. From their deflected shapes, they are actuated until their tip returns to the zero position of the initial state. As can be seen in the video, the parallel-tendon manipulator deforms further under the load, which agrees with our analytical results, and thus it takes much more tendon displacement to return the tip to its initial position. The video and Figure 8 show that it also cannot return to its straight, unloaded shape through actuation; the load causes the s-shape to remain even while actuated.

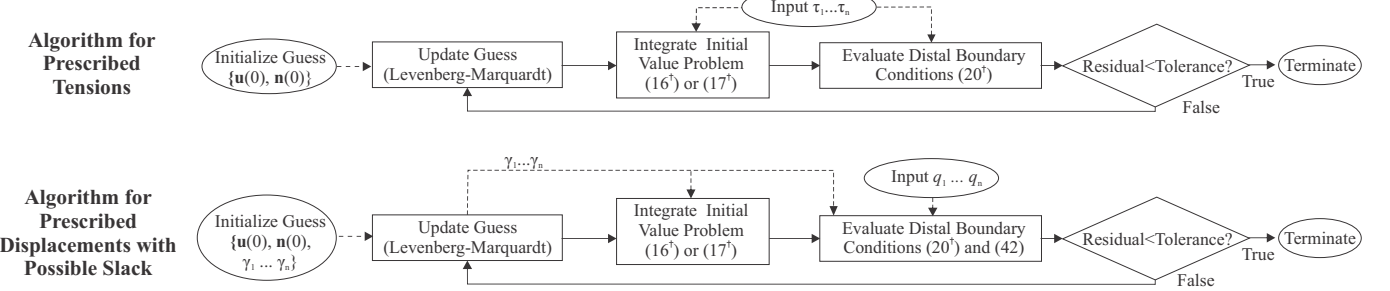


Fig. 9. These algorithmic flowcharts depict methods for solving the coupled Cosserat rod/tendon model equations subject to prescribed tendon tensions (top chart) or prescribed tendon displacements (bottom chart). The top chart is the approach described in [14], and equation numbers with the “†” symbol refer to that paper. The bottom chart method extends the model of [14] to prescribed tendon displacements with possible tendon slack by including new variables γ_i for the unknown slack/tension and additional constraint equations (42) to be satisfied.

Conversely, the converging-tendon manipulator deflects very little, requires less tendon displacement to return, and restores its original shape almost completely.

The choice of routing scheme offers clear differences in stiffness and shape, and it impacts other aspects of robot design, too. For example, parallel routing offers simpler construction for robots that embed tendons in a thin tube wall, which is commonly done; a true converging path as defined here cannot be attained in a robot with a central lumen since the tendon could not end at the centerline. However, the non-parallel linear path equations at the start of Section III describe the deflection of any compliant member with a linearly sloping tendon, which we call semi-converging, and such a manipulator is still stiffer overall as shown in Figure 6. Non-constant cross-sections could also be considered, and the approach taken in this paper can be adapted to the case where I is a function of arc length s .

IV. MODELING TENDON DISPLACEMENT INPUTS IN SPATIAL COSSERAT MODEL FRAMEWORK

The above analytical analysis is useful for small deflections from an initially straight robot shape, and the dimensionless deflection charts will help designers quickly evaluate the stiffness of candidate robot designs without significant modeling effort. However, high-magnitude external loads and initially curved actuated shapes invalidate the assumptions used. The true robot behavior will diverge from these analytical predictions as the robot gets further away from a nominal straight shape (whether due to actuation or external loads). To address this, we here extend the Cosserat rod model of tendon-driven robots in [14] to include prescribed tendon displacement inputs, tendon stretch, pretension, and slack. This nonlinear model framework is geometrically exact for all robot configurations and large loads. We will use the notation and conventions established in [14] for the sake of consistency.

In [14], the model inputs are prescribed tendon tensions and external loads, and the output is a framed 3D curve representing position and orientation of the backbone material. The top flowchart in Figure 9 depicts a typical shooting algorithm for solving the model equations. A guess for the values of the reaction forces at the base is iteratively updated

by a general purpose nonlinear solver (e.g. a Levenberg-Marquardt routine) in order to eventually satisfy the distal boundary conditions that the sum of forces and moments at the robot tip is zero for static equilibrium. In order to evaluate the boundary conditions, the differential equations describing the tendon robot [14] are integrated from base to tip using a standard routine for initial value problems (e.g. 4th order Runge-Kutta). The tendon tensions are inputs in the model in [14], and they appear in both the differential equations and the boundary conditions.

In the case of prescribed tendon displacements, the tendon tensions are initially unknown, and there are additional global length constraints that are dependent on the tendon displacements q_1, \dots, q_n , measured forward from the initial positions of the tendon bases. In the deformed manipulator state, the arc length s_i along a tendon guide path is implicitly a function of the unknowns $n(0)$, $u(0)$, and $\tau_1 \dots \tau_n$ through the following differential equation:

$$\dot{s}_i = \frac{ds_i}{ds} = \|\dot{\mathbf{p}}_i\| = \|\mathbf{u} \times \mathbf{r}_i + \dot{\mathbf{r}}_i + \mathbf{e}_3\|,$$

where $\mathbf{p}_i(s) \in \mathbb{R}^3$ is the global position of the i th tendon, $\mathbf{r}_i(s) \in \mathbb{R}^3$ is the tendon path location with respect to the robot centerline in the local frame (a predefined function), and $\mathbf{u} \in \mathbb{R}^3$ is the robot curvature vector in the local frame. Note that throughout this paper, a dotted variable indicates its derivative with respect to arc length, s . Integrating s_i along with the other state variables will give us the total path arc length $s_i(t_i)$ when the tendon terminates at $s = t_i$. The reference path length $s_{r,i}$ can be computed similarly using the reference curvature, and if the reference shape and guide paths are initially straight and parallel, then $s_{r,i}(t_i) = t_i$. By Hooke's law, and ignoring the possibility of slack, the tendon arc length $s_i(t_i)$ must be

$$s_i(t_i) = \begin{cases} \left(1 + \frac{\tau_i}{(EA)_i}\right) s_{r,i}(t_i) + q_i & (\text{extensible}) \\ s_{r,i}(t_i) + q_i & (\text{inextensible}) \end{cases} \quad (41)$$

where $(EA)_i$ is the tendon stiffness, τ_i is the unknown tendon tension, and q_i is a linear actuator displacement to retract the tendon. These equations must be enforced as an additional constraint to resolve the unknown tensions. Note, that in the special case of inextensible tendons, $(EA)_i \rightarrow \infty$, and the term in parentheses goes to 1. While the assumption

of inextensibility appears to eliminate tendon tension from the constraint equation, the tension is still implicitly involved as an unknown since the deformed path length s_i is a function of it, as shown in the equations of [14]. The algorithm framework depicted in Figure 9 is the same regardless of whether the tendons are stretchable, and we always solve for the unknown tendon tension that satisfies the appropriate constraint equation. Note that the simulations presented in Figures 1, 11(b) and (c), 17, and 18 all assumed inextensible tendons, while Figures 12, 13, 15, 14, and 16 considered compliant tendons, thus demonstrating the model's ability to handle both finite and infinite tendon stiffnesses.

In addition to tendon stretch, it is possible to develop slack in one or more tendons. If slack occurs the integrated path arc length $s_i(t_i)$ will be less than the actual tendon length. We can account for this by introducing an unknown variable β_i for the amount of slack. The length constraint is then

$$s_i(t_i) = \begin{cases} \left(1 + \frac{\tau_i}{(EA)_i}\right) s_{r,i}(t_i) + q_i - \beta_i & (\text{extensible}) \\ s_{r,i}(t_i) + q_i - \beta_i & (\text{inextensible}) \end{cases} \quad (42)$$

The inclusion of slack introduces an additional unknown variable for each tendon, but we can reduce the number of unknowns by recognizing that tendon tension and slack are mutually exclusive and restricted to be positive; that is, $\beta_i > 0 \implies \tau_i = 0$ and $\tau_i > 0 \implies \beta_i = 0$. Thus, we can represent both effects with a single unknown variable γ_i :

$$\begin{aligned} \tau_i &= \begin{cases} \gamma_i^2, & \gamma_i \geq 0 \\ 0, & \gamma_i < 0 \end{cases}, \\ \beta_i &= \begin{cases} 0, & \gamma_i \geq 0 \\ \gamma_i^2, & \gamma_i < 0 \end{cases}. \end{aligned} \quad (43)$$

Parameterizing tension and slack with a single, continuous variable eliminates the need to explicitly identify the appropriate constraints during model solves. The squaring of γ_i is a choice made so that τ_i and β_i have continuous first derivatives with respect to γ_i . The slack constraint residual error is most simply formulated as

$$E_i^s = s_i(t_i) + \beta_i - \left(1 + \frac{\tau_i}{(EA)_i}\right) s_{r,i}(t_i) - q_i,$$

but for better scaling of the shooting problem we implement the error as

$$E_i^{s^*} = (1 + \tau_i) E_i^s.$$

This seems to result in better solver convergence, and we note that the $(1 + \tau_i)$ term will never nullify E_i because τ_i is positive semidefinite.

For a robot with n tendons, our approach provides the right number of equations to solve for the $6 + n$ unknowns: $\mathbf{u}(0)$, $\mathbf{n}(0)$, and $\gamma_1 \dots \gamma_n$, where $\mathbf{n}(s) \in \mathbb{R}^3$ is the internal force of the backbone. To do this, we modify the shooting algorithm as shown in the bottom flow chart in Figure 9. The tension/slack variables $\gamma_1 \dots \gamma_n$ are simply appended to the set of unknowns that is iteratively updated and obtained by the Levenberg-Marquardt routine. The iteratively updated variables are all used in the differential equations and boundary

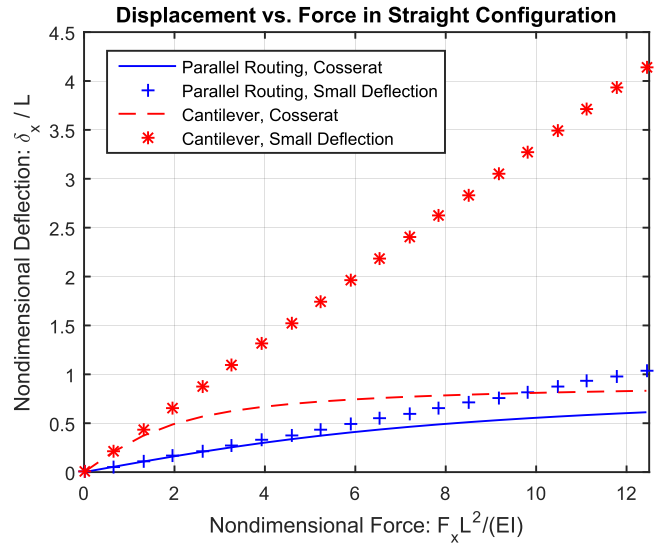


Fig. 10. The analytical formulas of Section II are a good approximation for initially straight robot shapes under small loads. At larger loads and significantly curved actuated shapes, the nonlinear Cosserat model should be used.

condition evaluations, which now include the new constraints in (41) based on the prescribed displacements $q_1 \dots q_n$.

A. Comparison of Analytical Formula to Cosserat Model

As an example, Figure 10 compares the results of the small-deflection analytical model to the large-deflection 3D model developed in this section for an initially straight robot shape. The large-deflection scenarios are not captured well by the analytical formulas, which motivates the development of the extended Cosserat model in this section.

B. Spatial Simulation and Discussion

Before providing non-dimensional displacement charts based on the Cosserat model, we illustrate the use of our new approach in three simulations computed using the methods described above and rendered in Figure 11. The simulated robot was modeled with an incompressible backbone (Kirchhoff rod) of length $L = 0.1\text{m}$, diameter 1.04mm , Young's modulus $E = 210\text{GPa}$ and shear modulus $G = 80\text{GPa}$, and three equally spaced parallel tendons with guide channels offset $r = 0.01\text{m}$ from the centerline. Computation time using an unoptimized MATLAB implementation on a standard laptop computer with i7 processor is typically the order of 1 second or less, depending on how close the initial guess is to the solution, but note that optimized implementations of Cosserat rod models can run in real-time as demonstrated in [30]. Figure 11 (a) and (b) show a manipulator actuated to a 90° tip angle by inextensible tendons. Transverse and vertical loads are then applied, and the plot compares the resulting deformed shape in the case of prescribed displacements and prescribed constant tension. This affirms the main conclusion of our analytical results of previous sections and extends it to the actuated case: prescribed tendon displacements significantly increase the output stiffness.

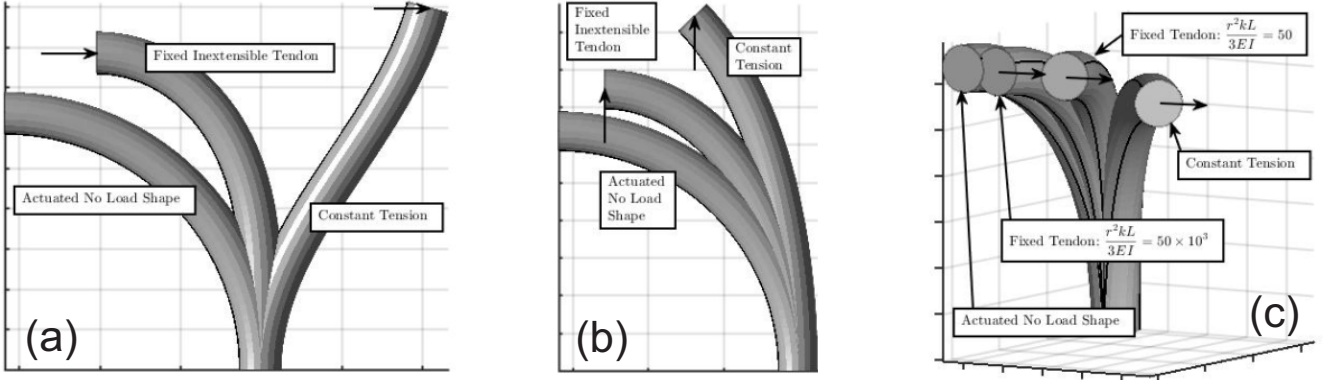


Fig. 11. In each plot, simulations of tendon-driven manipulators are shown where the initial actuated tip angle is 90° . A load is applied, and the resulting displacements are calculated and compared using both prescribed tensions and prescribed displacements. (a) and (b) show single-inextensible tendons manipulators with in-plane loads while (c) has three evenly-spaced, stretchable tendons with an out of plane load.

C. Sensitivity to Tendon Stiffness in Special Loading Cases

We now use our model to illustrate the fact that in certain special cases, even a very small amount of tendon stretch can significantly affect a robot's loaded shape. In Figure 11 (c), we simulate an out-of-plane load applied to the same initial configuration with three symmetrically spaced, stretchable tendons. The out-of-plane loading causes torsion as well as bending, and the torsion is a significant contributor to the overall shape and amount of tip deflection. However, torsion has a minimal effect on the stretch of individual tendons. These two observations imply that only highly stiff tendons can mitigate the significant torsional effects caused by out-of-plane loads, and this is illustrated in the plot. For the in plane loads, increasing the dimensionless tendon stiffness beyond $\frac{r^2 k L}{3EI} = 50$ has a negligible effect, but in the out-of-plane load case, the plot shows a significant deflection difference between $\frac{r^2 k L}{3EI} = 50$ and $\frac{r^2 k L}{3EI} = 50 \times 10^3$. Since robots encounter such loads in many practical scenarios, this example underscores the importance of actually modeling the tendon stretch (and/or similar effects such as backbone compression) in order to accurately predict robot performance.

Further, we can conceive another a special case in which tendon inextensibility actually creates a paradox. Figure 12 considers three straight tendons on a straight, incompressible backbone subjected to a pure axial moment at the tip. If we keep increasing the tendon stiffness, the torque/displacement curve becomes more nonlinear, and we see larger resistance for finite displacements, but the slope at zero is apparently unaffected. In the limit as tendon stiffness approaches infinity, the member cannot exhibit any finite angular displacement (since any angular displacement of the tip must either elongate the tendons or compress the backbone), yet the slope of the torque/displacement curve at zero remains constant, and if there is zero angular displacement, geometry dictates that neither the backbone material nor the tendons can possibly provide a resistance torque to balance the applied moment, creating a singular paradox. This again shows the importance of modeling tendon and backbone compliance, even if they are small, in order to avoid singularities introduced by assuming

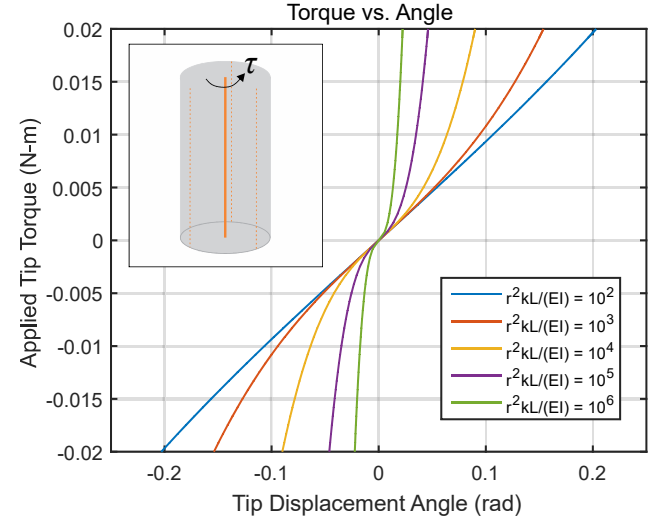


Fig. 12. A torque is applied at the end effector of a three-tendon robot with an incompressible backbone in the straight configuration. There is a singularity $\lim_{c \rightarrow 0} \partial\theta / \partial\tau = 0$. Interestingly, the slope at $\theta = 0$ is constant regardless of the tendon compliance.

zero axial strain in both the backbone and tendons.

D. Dimensionless Deflection Plots for the 3D Actuated Case

We now provide dimensionless stiffness plots for a typical 3D actuated case, analogous to the analytical results using the planar small-deflection assumptions in the previous section. These plots are generated by the Cosserat model with parameters given in the previous section and for a robot actuated to a 90° tip angle and subjected to loads in the transverse (horizontal) direction in the bending plane, the axial (vertical) direction in the bending plane, and loads orthogonal to the bending plane (out-of-plane), as depicted by the force arrows in the Figures below. Following the discussion in the previous section, we note that poor numerical conditioning in the case of inextensible tendons caused convergence issues in some cases, so a high dimensionless stiffness of 8.29×10^6 was used instead. Figures 13, 15, and 14 show the dimensionless

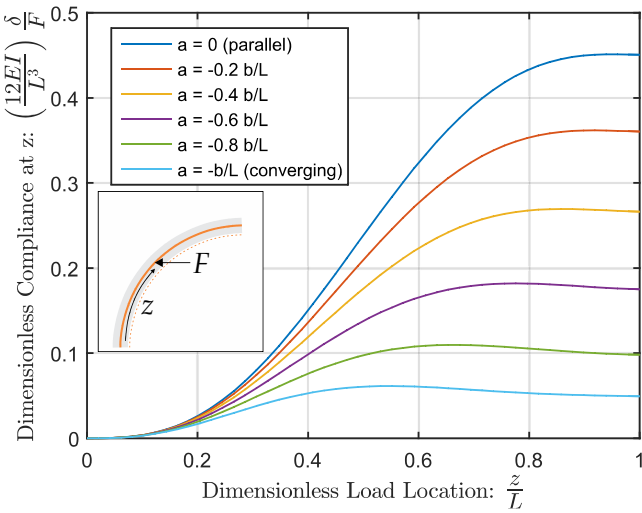


Fig. 13. This plot shows the dimensionless compliance for forces applied in the transverse in-plane direction for a robot actuated so that the tip is bent 90° . The dimensionless tendon stiffness is 8.29×10^6 .

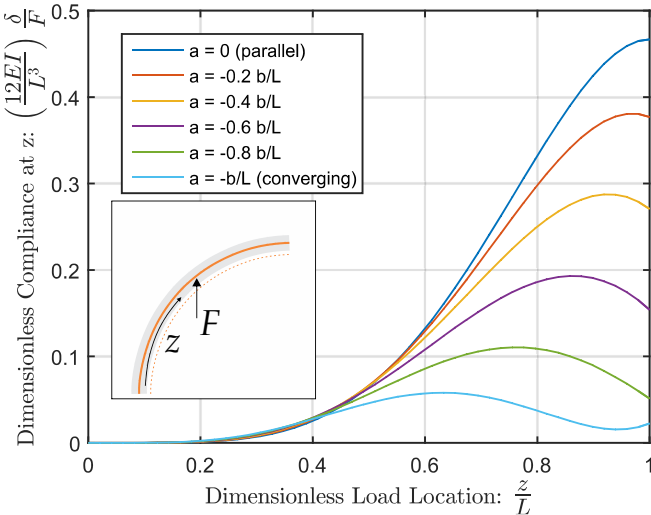


Fig. 14. This plot shows the dimensionless compliance for forces applied in the axial in-plane direction for a robot actuated so that the tip is bent 90° . The dimensionless tendon stiffness is 8.29×10^6 .

compliance (for small loads) at a loaded point z in each load direction (transverse, axial, and out-of-plane). As in the previous analytical results, the robot's stiffness increases with converging tendon routing, except in the out-of-plane load, where the routing path seems to have a negligible effect.

The effect of tendon stiffness in the 3D model is further examined in Figure 16, which shows the relationship of tendon stiffness to tip compliance in the three directions for a robots with a single tendon (in both parallel and converging cases) actuated to a 90° tip angle. For the axial loading direction, the converging tendon design results in greater tip stiffness if the dimensionless tendon stiffness is larger than 15. For the transverse loading direction, the converging design is stiffer for all tendon stiffnesses. The effect of tendon stiffness and routing path for loads in the out-of-plane direction is nearly imperceptible, but the results from the simulations in Figure

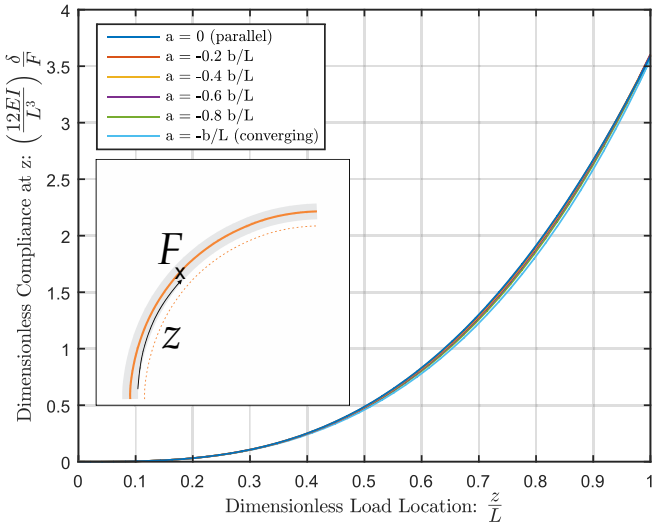


Fig. 15. This plot shows the dimensionless compliance for forces applied in the out-of-plane direction for a robot actuated so that the tip is bent 90° . The dimensionless tendon stiffness is 8.29×10^6 .

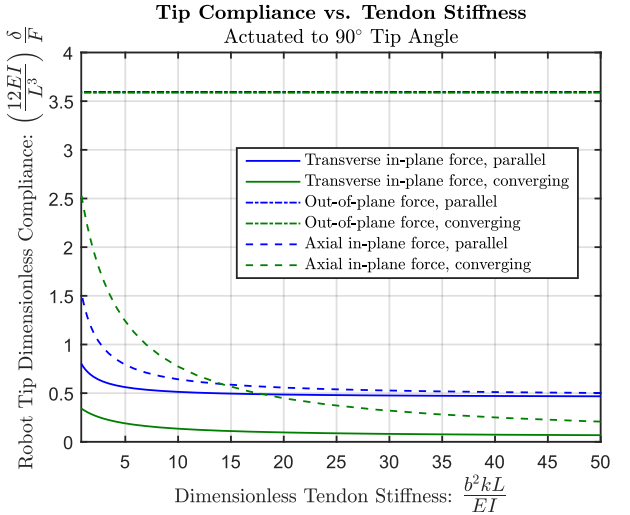


Fig. 16. This chart shows simulated results for the robot tip compliance versus dimensionless tendon stiffness for both parallel and converging designs in the 3D case where the robots are actuated to a 90° tip angle and subjected to loads in the axial, transverse, and out-of-plane directions. The results with the spatial rod model match the analytical results in Figure 7.

11 suggest that these lines do have a small slope.

E. Simulation with Slack

We also provide an example simulation where a tendon becomes slack during external loading by implementing the methods described in this section. In certain circumstances, it is possible for external loads to induce tendon slack, and this can significantly affect the displacement. While robots with opposing tendons can generally avoid slack by employing a fixed amount of pretension, robot segments with a single tendon or with tendons only on one side have no redundancy available for pretension to exploit, and thus slack is more likely to occur. Such a scenario is illustrated in Figure 17. An incompressible robot backbone has a single inextensible tendon with a prescribed displacement such that the tip is

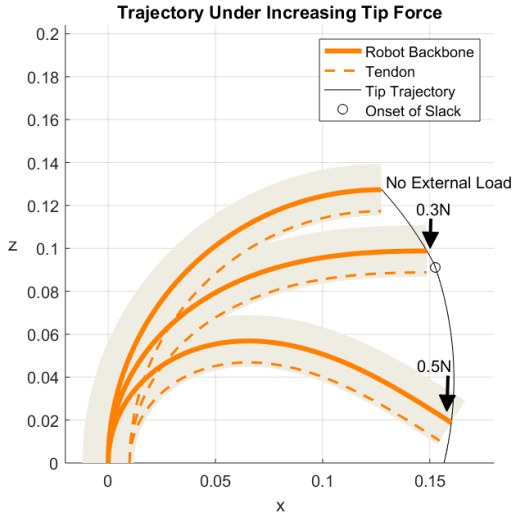


Fig. 17. A simulated tendon robot is actuated to 90° , and the actuator position is locked. Initially, the robot maintains its orientation under an increasing tip force, but a sufficiently large tip force results in tendon slack, and the orientation is no longer constrained. After the load induces tendon slack, the tip compliance is about 3 times greater than when the tendon was taught.

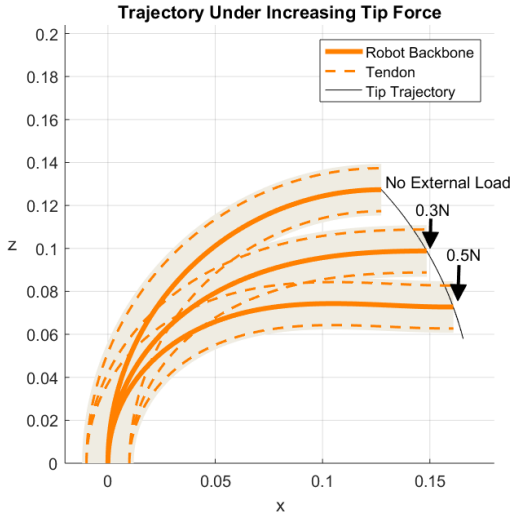


Fig. 18. Repeating the simulation of Figure 17 with an additional opposing tendon yields a drastically different result. Due to a constant pretension, both tendons remain in tension and continue to constrain the tip orientation to 90° resulting in much less displacement at 0.5 N.

brought to a 90° angle. When a vertical external load is applied, the tendon initially remains in tension, and the tip angle remains at 90° while the tip displaces downward. Above the critical load of 3.6N, the tendon tension goes to zero, slack is induced, and the tip is free to rotate. In the induced-slack regime, the compliance at the tip is a factor of 3 higher than it was when the tendon remained in tension. To illustrate the benefit of employing opposing tendons, the same simulation experiment is shown in Figure 18 with two opposing tendons and enough pretension to avoid the load-induced slack in the shorter tendon. The avoidance of slack results in a significantly smaller deflection at 0.5N and constant tip orientation throughout the loading.

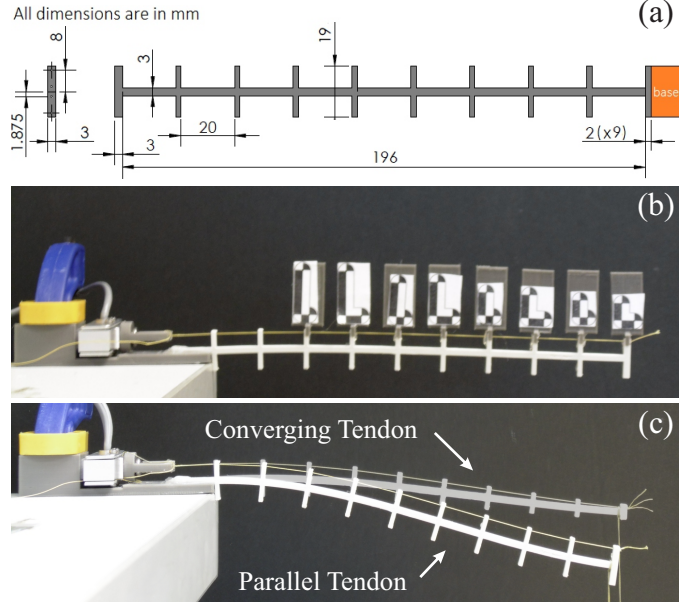


Fig. 19. Shown are the tendon-embedded structures, dimensioned in (a), used in the experimental validation of the analytical models, where the loads were applied at eight evenly spaced points along the member length (the inner corners of the 8 most distal tendon supports). The radial offset in (a) is the offset for the parallel tendon structure and the initial offset in the converging structure, and the terminal offset for the converging tendon is also shown. The markers used to track deflection are shown in (b), and the overlaid image in (c) shows both structures under a 0.5N tip load; the parallel-routed member deflects around twice as much as the converging-routed one.

For the simulations used to generate Figures 17-18, the robot backbone length is $L = 0.2\text{m}$ and the tendon offset is 0.01m. The Young's modulus and shear modulus are 207GPa and 79.6GPa respectively, and the diameter of the backbone is 0.8mm.

V. VALIDATION OF MODELS

A. Validation of 2D Analytical Models

We have validated the formulas from Sections II and III in a set of experiments where known weights were hung from a cantilevered elastic member with tendon guide channels, shown in Figure 19, for both a member with parallel tendon routing and one with converging tendon routing. Aside from the tendon paths, the members and experimental procedures were identical between the two routing cases, and the dimensions are provided in Figure 19(a). They were 3D printed using Amphora ColorFabb HT on a MakeIt-Pro M printer. The members had a square cross section of 3 mm side length. Ten evenly spaced, tendon guides were added with tendon routing holes at a radius of 8 mm from the centerline for the parallel tendon case and holes beginning at the base with a radius of 8 mm and ending at the tip with a radius of 1.875 mm for the converging case. The tendon guide on the tip was 3 mm thick to mitigate deformation of the support at the point at where the tendons were attached, and all others were 2 mm thick, making the total length 201 mm. Ending the converging tendon exactly at the centerline (as specified in Section III) would diminish the structural integrity of the tip, as the tendon hole would have cut through the member's cross-section, so instead, the distal

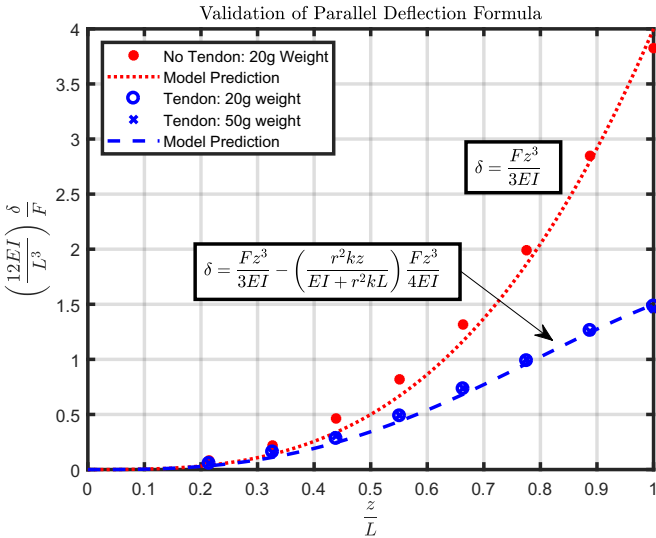


Fig. 20. Data from the loading experiments for the parallel routing case are shown with the curves of the analytical formulas.

end of the converging tendon was terminated with the smallest offset from the centerline that could be created without cutting through the member. We installed a single tendon (size 69 Kevlar thread) through the top set of guides on each member.

For each routing case, we performed eight baseline measurements with no tendon attached, measuring the deflection due to a 20-gram calibration weight hung at various locations along the robot length. The load locations were at evenly spaced points along the member (i.e. at each tendon guide except the two closest to the base). Unique markers were attached to each of the tendon guides that were used in the loading as shown in Figure 19(b), and a MicronTracker (Claron Technology, USA) was used to capture displacement data at all 8 points on the member for each load. We calibrated the effective flexural rigidity EI of the member by performing a least squares fit of the data from these 8 displacement experiments. The result is shown by the red dashed line in Figures 20 and 21. In the parallel tendon case, the resulting calibrated rigidity of $EI = 11.2 \times 10^3 \text{ N mm}^2$ was just over 5% higher than the nominal value computed from the cross section dimensions and an E of 1.575 GPa for ColorFabb HT. In the converging tendon case, the calibrated rigidity was found to be $EI = 11.3 \times 10^3 \text{ N mm}^2$, which is just 6% higher than the nominal value.

Next, we rigidly attached the tendons to an Omega LC70 3-10 load cell with a 3D printed bracket, pulling the tendon taught enough to avoid slack while not inducing bending in the structure before fixing it to the bracket. The force data was read using a SparkFun Load Cell Amplifier HX711 and an Arduino Mega 2560, and the readings were streamed through the Arduino IDE serial monitor. The load cell was then anchored to a rigid base, and we performed the same eight displacement tests on both members, except a 50g weight was used to apply the forces. To calibrate each effective tendon spring constant k , we performed a least squares fit of the data from these 8 experiments for each member, using its previously calibrated

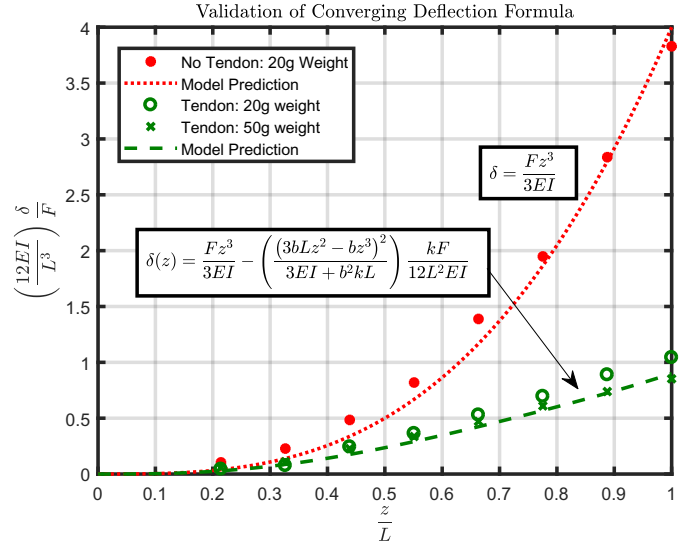


Fig. 21. Experimental data for the converging routing case is shown alongside the curve for the analytical formula. The tendon-less member data that was used for the calibration of EI is shown in red.

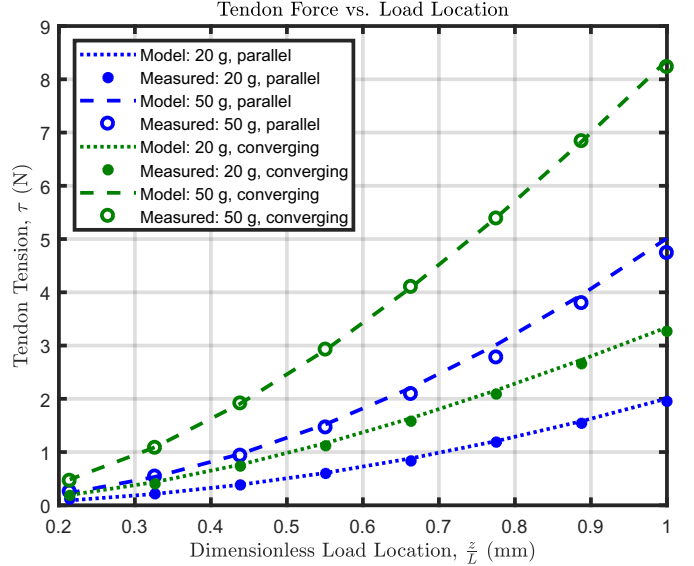


Fig. 22. For each applied load and load location, the tendon tension was measured. The model-predicted curves use Equations (6) and (25), which do not account for friction, and the calibrated EI and k values from the experiment. These results show that friction can be safely neglected for the model of our setup, at least in the initially straight case. As the robot becomes more curved, friction plays an increasing role as indicated by Figure 25

value of EI . The resulting prediction is compared to the data in Figures 20, 21, and 23. For the member with a parallel tendon, the calibrated value of k was 4.5 N/mm, resulting in the nondimensional parameter $\frac{r^2 k L}{EI} = 5.03$. We note that the actual Kevlar thread has a much higher stiffness than this calibrated value, so the calibration is likely accounting for other factors that create an effect similar to a reduced tendon stiffness, such as finite clearance between the tendon and the guide holes, axial compression of the central backbone (which we showed in Section II can be modeled by an effective tendon stiffness), and compliance of other structures such as the tendon guide where the tendon was fixed at the tip. For

the member with a converging tendon, the calibrated tendon stiffness was $k = 8.55$ N/mm (making for a dimensionless tendon stiffness of 9.52). The effective stiffness is lower in the parallel routing case due to a small amount of bending in the final tendon guide where the tendon is fixed at the tip. In the converging case, there is practically no bending in the final guide because the moment arm is nearly zero, another advantage of the converging tendon design that affects stiffness.

Finally, we cross-validated the performance of our calibrated model on a third, independent set of 8 data points for each robot, which were generated with a different weight (20g) hung at each point on both members with fixed tendon displacements. These data agreed with the prediction of the model using the two previously calibrated parameters EI and k , as shown in Figure 20 (parallel tendons) and Figure 21 (converging tendons). The tendon force data, averaged from 100 points taken during each loading scenario, can be seen in Figure 22. The predicted model again uses the calibrated EI and k , and the measured tensions follow closely to the prediction. If friction were a significant factor, the measured tension would be much different from our model prediction, as we do not account for it; thus, the tension measurements illustrate that our assumption of neglecting friction is valid for our test system.

Figure 23 shows the experimental data from the 20-gram and 50-gram weights superimposed on the theoretical manipulator shapes for the last four loading cases in Cartesian space. Integration of the sine and cosine of theta (Equations (3) and (22) with their respective equations for τ substituted in) with respect to arc length produces the theoretical curve in each case. These equations also used the respective calibrated EI and k values from the experiment for the parallel and converging shapes. The plotted experimental data points show the measured deflection in the y-axis of the eight tracked points at the appropriate x location calculated by integration to the load arc length. The plots demonstrate the loaded shape differences between the two routing paths; the parallel path produces an s-shape when deflected, and the converging tendon path produces smaller deflection along the entire length of the manipulator than the parallel path for the same load. In particular, the converging tendon design is shown to be stiffer than the parallel design by a factor of two, which is consistent with the deflection formulas and the gains predicted by Figure 7 at the calibrated effective tendon stiffnesses.

B. Validation of 3D Model for In-Plane Loads

We also validated the 3D numerical Cosserat model using members of the same geometry and fabrication method as the prior experiments. A motor mount structure was made with 3D printed parts, and Dynamixel MX-28 servo motors were used to actuate each member using a single tendon, as shown in Figure 24. Tests were carried out with the robots at a 30° and 60° tip angle. The motor was gripped in a vice and clamped to the table to ensure stability. A tracking marker was placed on the tip and at the base of the robot in order to measure tip deflection in the robot base frame. The MicronTracker was

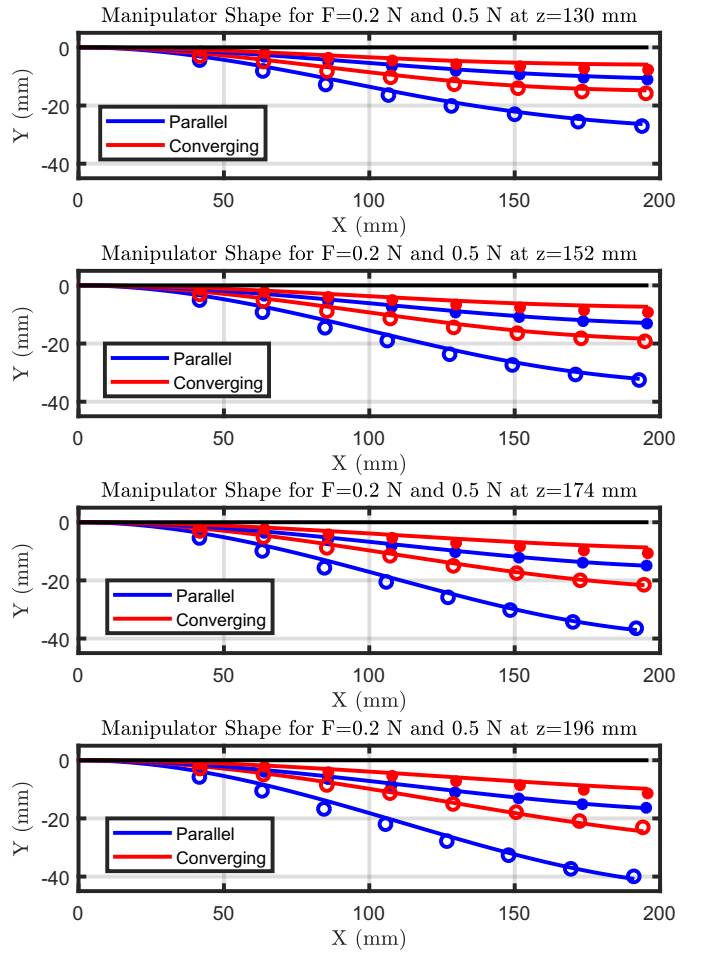


Fig. 23. Shown here are the shapes of parallel- and converging-routed prototypes when loaded at different points along the manipulator. For a load of 0.2 N and 0.5 N on each manipulator, the shape was found by integrating the equations for $\theta(s)$ with respect to arc length. The circles on each plot represent the experimental data of the y-displacement of the measured points plotted at the correct arc length; the solid circles are the 0.2 N data, and the rings are the 0.5 N data.

used to capture displacement data as the tip was loaded in the axial (vertical) direction using weights of 10 to 50 grams in 10-gram increments. The direction of loading was such that tendon slack could develop, but it was not observed at these magnitudes of tip forces. The deflection data is shown in Figure 25.

The frictionless model predicts the deflection well for the tests carried out at a 30° tip angle and slightly less accurately in the 60° actuated case. While the predicted stiffness difference between the parallel and converging cases is well matched, the data shows slightly stiffer behavior than the model prediction. This discrepancy is likely due to the stiffening effects of static friction between the guide holes and the tendon, which is not considered in our models. We note that these robots were not specifically designed to minimize tendon channel friction. The further the robot is actuated, the more pronounced frictional effects will be, so designs that are intended for larger ranges of motion may benefit from lubricious materials for the tendon channels or friction-reducing coatings. The effects of static friction can

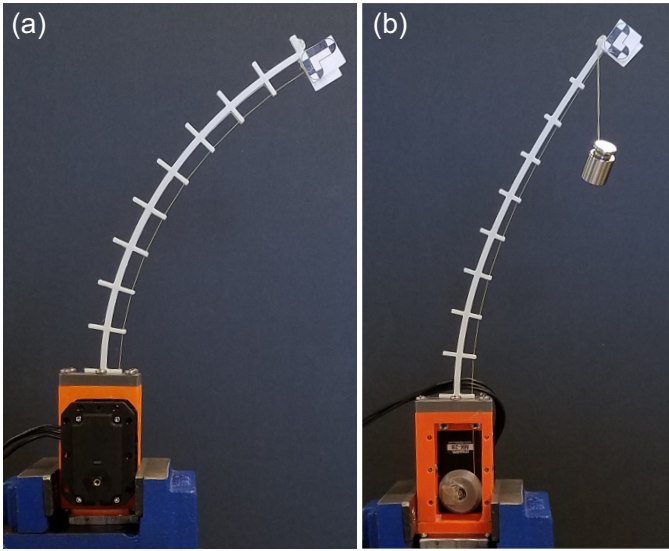


Fig. 24. The robots were actuated to 30° and 60° and loaded. The parallel robot is shown in (a) unloaded, and (b) shows the converging-routed robot under a 0.2-N load, both actuated to a 60° tip angle.

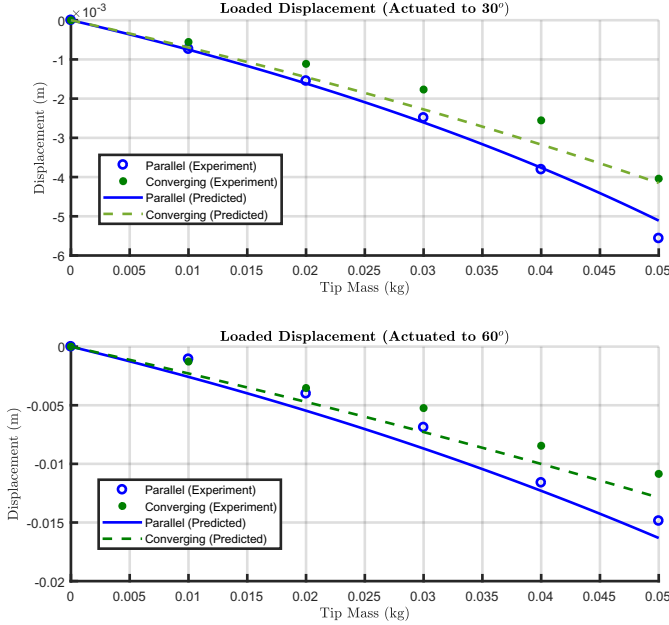


Fig. 25. The robots were actuated to 30° and 60° tip angles and loaded in the axial direction. The results agree well with our model prediction for the 30° case, but friction in the 60° case causes slightly less deflection than predicted. This points to the need for including friction when lubricious materials or friction-reducing coatings are unavailable for robots that are actuated to high angular displacements.

also potentially be reduced by “dithering” during robot control as described in [11].

VI. CONCLUSIONS AND LIMITATIONS

This paper has explored the behavior of continuum robots driven by prescribed tendon displacements under external loads. Using Bernoulli-Euler beam equations, we derived analytical equations for the loaded deflections of a compliant member embedded with one or more tendons. This provided

useful insight into the role of tendon stretch, backbone compression, and tendon location on the overall stiffness. We additionally investigated non-parallel routing paths and showed that using a converging tendon path can significantly increase the stiffness of the member along its entire length, though it also increases the required actuation force for tip articulation and induces a shape with linearly varying curvature. We believe that the effects of non-parallel tendon routing can be exploited to improve continuum robot design by creating stronger, more controllable robots, and we hope that the results herein will serve designers well as a tool for selecting design parameters and control schemes.

To account for large-deflection scenarios, we extended the general Cosserat rod / tendon model to accept prescribed tendon displacement inputs, which is useful for simulating the majority of tendon-driven manipulators, which are tendon-displacement controlled. The model extension also newly accounts for tendon slack, stretch, and pretension. Simulations show that accurately predicting out-of-plane loading requires modeling the tendon stretch, and that load-induced slack can increase compliance. We used the extended model to generate numerically-simulated results for nondimensional compliance in x, y, and z directions along the length of an actuated robot with various tendon routings. Similarly, we explored how the nondimensional tendon stiffness affects the compliance of an actuated robot in all three directions for parallel and converging routing schemes. Finally, we validated the analytical models with a set of experiments using a 3D-printed member, an optical tracking system, a force sensor, and known weights, showing that friction is negligible when considering small deflections from an initially straight shape. We validated the Cosserat model using position-dictated actuation for two actuated shapes (30° and 60° tip angle) and 5 external load magnitudes. The results showed that the model, which does not include friction, predicts the externally-loaded shape of the robot well when actuated to 30° , but friction plays a larger role as curvature increases, and the results for 60° agree well but begin to display the limitations of our model.

One limitation of this study has been that we neglected static tendon friction in all the models and analysis for the sake of tractability. Static friction can effectively stiffen a tendon-driven robot, and this effect is greater at larger tensions and configurations with higher curvatures, as our experimental results showed. Modeling and estimation of tendon friction in robots without external loads has been recently addressed in [31], and those results may eventually be adaptable to models with external loading in the future.

REFERENCES

- [1] D. Trivedi, C. D. Rahn, W. M. Kierb, and I. D. Walker, “Soft Robotics: Biological Inspiration, State of the Art, and Future Research,” *Applied Bionics and Biomechanics*, vol. 5, no. 3, pp. 99–117, sep 2008.
- [2] R. J. W. III and B. A. Jones., “Design and Kinematic Modeling of Constant Curvature Continuum Robots: A Review,” *International Journal of Robotics Research*, 2010.
- [3] I. D. Walker, “Continuous Backbone Continuum Robot Manipulators,” *ISRN Robotics*, vol. 2013, pp. 1–19, 2013.
- [4] J. Burgner-Kahrs, D. C. Rucker, and H. Choset, “Continuum Robots for Medical Applications: A Survey,” *IEEE Transactions on Robotics*, vol. 31, no. 6, pp. 1261–1280, dec 2015. [Online]. Available: <http://ieeexplore.ieee.org/lpdocs/epic03/wrapper.htm?arnumber=7314984>

- [5] T. D. Nguyen and J. Burgner-Kahrs, "A tendon-driven continuum robot with extensible sections," *IEEE International Conference on Intelligent Robots and Systems*, vol. 2015-December, pp. 2130–2135, 2015.
- [6] T. Kato, I. Okumura, S. E. Song, A. J. Golby, and N. Hata, "Tendon-Driven Continuum Robot for Endoscopic Surgery: Preclinical Development and Validation of a Tension Propagation Model," *IEEE/ASME Transactions on Mechatronics*, vol. 20, no. 5, pp. 2252–2263, 2015.
- [7] M. D. M. Kutzer, S. M. Segreti, C. Y. Brown, M. Armand, R. H. Taylor, and S. C. Mears, "Design of a new cable-driven manipulator with a large open lumen: Preliminary applications in the minimally-invasive removal of osteolysis," in *IEEE International Conference on Robotics and Automation*, no. Dm, 2011, pp. 2913–2920.
- [8] I. D. Walker, "Robot Strings : Long , Thin Continuum Robots," in *IEEE Aerospace Conference*, 2013, pp. 1–12.
- [9] M. M. Tonapi, I. S. Godage, and I. D. Walker, "Next generation rope-like robot for in-space inspection," in *2014 IEEE Aerospace Conference*, March 2014, pp. 1–13.
- [10] J. Reinecke, B. Deutschmann, and D. Fehrenbach, "A structurally flexible humanoid spine based on a tendon-driven elastic continuum," *Proceedings - IEEE International Conference on Robotics and Automation*, vol. 2016-June, pp. 4714–4721, 2016.
- [11] D. Camarillo, C. Milne, C. Carlson, M. Zinn, and J. Salisbury, "Mechanics Modeling of Tendon-Driven Continuum Manipulators," *IEEE Transactions on Robotics*, vol. 24, no. 6, pp. 1262–1273, dec 2008.
- [12] I. A. Gravagne, C. D. Rahn, and I. D. Walker, "Large-Deflection Dynamics and Control for Planar Continuum Robots," *IEEE/ASME Transactions on Mechatronics*, vol. 8, no. 2, pp. 299–307, jun 2003.
- [13] B. A. Jones, R. L. Gray, and K. Turlapati, "Three dimensional statics for continuum robotics," in *2009 IEEE/RSJ International Conference on Intelligent Robots and Systems*. IEEE, oct 2009, pp. 2659–2664.
- [14] D. C. Rucker and R. J. Webster III, "Statics and Dynamics of Continuum Robots With General Tendon Routing and External Loading," *IEEE Transactions on Robotics*, vol. 27, no. 6, pp. 1033–1044, dec 2011.
- [15] W. S. Rone and P. Ben-Tzvi, "Continuum Robot Dynamics Utilizing the Principle of Virtual Power," *IEEE Transactions on Robotics*, vol. 30, no. 1, pp. 275–287, feb 2014.
- [16] F. Renda, M. Giorelli, M. Calisti, M. Cianchetti, and C. Laschi, "Dynamic Model of a Multibending Soft Robot Arm Driven by Cables," *IEEE Transactions on Robotics*, vol. 30, no. 5, pp. 1109–1122, oct 2014.
- [17] M. S. Moses, R. J. Murphy, M. D. M. Kutzer, and M. Armand, "Modeling Cable and Guide Channel Interaction in a High-Strength Cable-Driven Continuum Manipulator," *IEEE/ASME Transactions on Mechatronics*, vol. 20, no. 6, pp. 2876–2889, dec 2015.
- [18] H. Yuan and Z. Li, "Workspace analysis of cable-driven continuum manipulators based on static model," *Robotics and Computer-Integrated Manufacturing*, vol. 49, pp. 240–252, 2018.
- [19] J. Back, L. Lindenroth, R. Karim, K. Althoefer, and K. Rhode, "New Kinematic Multi - Section Model for Catheter Contact Force Estimation and Steering," *2016 IEEE/RSJ International Conference on Intelligent Robots and Systems (IROS)*, pp. 2122–2127, 2016.
- [20] J. Back, L. Lindenroth, K. Rhode, and H. Liu, "Model-Free Position Control for Cardiac Ablation Catheter Steering Using Electromagnetic Position Tracking and Tension Feedback," *Frontiers in Robotics and AI*, vol. 4, p. 17, may 2017.
- [21] B. A. Jones and I. D. Walker, "Kinematics for Multisection Continuum Robots," *IEEE Transactions on Robotics*, vol. 22, no. 1, pp. 43–55, 2006.
- [22] ——, "Practical Kinematics for Real-Time Implementation of Continuum Robots," *IEEE Transactions on Robotics*, vol. 22, no. 6, pp. 1087–1099, 2006.
- [23] I. A. Gravagne and I. D. Walker, "Manipulability, force, and compliance analysis for planar continuum manipulators," *IEEE Transactions on Robotics and Automation*, vol. 18, no. 3, pp. 263–273, 2002.
- [24] K. C. Lau, E. Y. Y. Leung, P. W. Y. Chiu, C. Y. Yam, J. Y. W. Lau, and C. C. Y. Poon, "A Flexible Surgical Robotic System for Removal of Early-Stage Gastrointestinal Cancers by Endoscopic Submucosal Dissection," *IEEE Transactions on Industrial Informatics*, vol. 3203, no. c, pp. 1–1, 2016. [Online]. Available: <http://ieeexplore.ieee.org/lpdocs/epic03/wrapper.htm?arnumber=7484685>
- [25] B. L. Conrad, J. Jung, R. S. Penning, and M. R. Zinn, "Interleaved Continuum-Rigid Manipulation : An Augmented Approach For Robotic Minimally-Invasive Flexible Catheter-based Procedures," in *IEEE International Conference on Robotics and Automation*, 2013, pp. 710–716.
- [26] D. B. Camarillo, C. R. Carlson, and J. K. Salisbury, "Configuration Tracking for Continuum Manipulators With Coupled Tendon Drive," *IEEE Transactions on Robotics*, vol. 25, no. 4, pp. 798–808, 2009.
- [27] T. Kato, I. Okumura, H. Kose, K. Takagi, and N. Hata, "Extended kinematic mapping of tendon-driven continuum robot for neuroendoscopy," in *Proceedings of the 2014 IEEE/RSJ International Conference on Intelligent Robots and Systems, IROS 2014, September 14-18, 2014*, 2014, pp. 1997–2002.
- [28] Y.-J. Kim, S. Cheng, S. Kim, and K. Iagnemma, "A Stiffness-Adjustable Hyperredundant Manipulator Using a Variable Neutral-Line Mechanism for Minimally Invasive Surgery," *IEEE Transactions on Robotics*, vol. 30, no. 2, pp. 382–395, apr 2014.
- [29] A. Shiva, A. Stilli, Y. Noh, A. Faragasso, I. D. Falco, G. Gerboni, M. Cianchetti, A. Menciassi, K. Althoefer, and H. A. Wurdemann, "Tendon-Based Stiffening for a Pneumatically Actuated Soft Manipulator," *IEEE Robotics and Automation Letters*, vol. 1, no. 2, pp. 632–637, jul 2016.
- [30] J. Till, C. E. Bryson, S. Chung, A. Orekhov, and D. C. Rucker, "Efficient computation of multiple coupled Cosserat rod models for real-time simulation and control of parallel continuum manipulators," in *IEEE International Conference on Robotics and Automation (ICRA)*, 2015, pp. 5067–5074.
- [31] R. Roy, L. Wang, and N. Simaan, "Modeling and Estimation of Friction, Extension, and Coupling Effects in Multisegment Continuum Robots," *IEEE/ASME Transactions on Mechatronics*, vol. 22, no. 2, pp. 909–920, apr 2017.